J Sol-Gel Sci Technol (2011) 59:290–296
DOI 10.1007/s10971-011-2498-4

ORIGINAL PAPER

Strong up conversion photoluminescence in Er^{3+} doped $Bi_4Ti_3O_{12}$ ferroelectric materials prepared by sol–gel method

H. W. Zheng · S. J. Liu · G. S. Yin · W. C. Wang · C. L. Diao · Y. Z. Gu · W. F. Zhang

Received: 15 February 2011 / Accepted: 16 May 2011 / Published online: 28 May 2011

Abstract $Bi_4Ti_3O_{12}$ (BTO) doped with different concentrations of Er^{3+} was prepared using sol–gel method. Their structures and surface morphology were examined by X-ray diffraction, Raman spectroscopy and scanning electron microscopy, respectively. All XRD peaks can be indexed according to orthorhombic BTO phase, which is consistent with Raman measurement results. Strong upconversion green luminescence is observed in the Er^{3+} doped BTO powders pumped by 980 nm at room temperature. Three upconversion emission bands centered at about 525, 550 and 662 nm are due to the radiative relaxation of Er^{3+} from $^2H_{11/2}$, $^4S_{3/2}$ and $^4F_{9/2}$ to the ground level $^4I_{15/2}$, respectively. The upconversion emission mechanism of the samples were identified and analyzed. In addition, the doped BTO ceramics show obvious hysteresis loops, demonstrating the ferroelectric properties of the samples. These results illustrate the potential of this class of materials for photonic applications in optoelectronics devices.

Keywords Bismuth layer-structured · Ferroelectrics · Doping · Up-conversion photoluminescence · Sol–gel

H. W. Zheng (✉) · G. S. Yin · W. C. Wang · C. L. Diao · Y. Z. Gu · W. F. Zhang (✉)
Department of Physics, Institute of Microsystem, Key Laboratory of Photovoltaic Materials, Henan University, Kaifeng 475004, People's Republic of China
e-mail: zhenghaiwu76@yahoo.com.cn

W. F. Zhang
e-mail: wfzhang@henu.edu.cn

S. J. Liu
Department of Physics, Luoyang Normal University, Luoyang 471002, China

1 Introduction

$Bi_4Ti_3O_{12}$ (BTO), a kind of bismuth layer structure ferroelectrics, has emerged as highly promising materials in nonvolatile ferroelectric random access memory and high temperature piezoelectric devices because of their low dielectric constant, high Curie temperature and excellent fatigue-free properties [1]. Rare earth doped BTO ferroelectric materials have been intensively investigated for their applications in optoelectronics and microelectronics [2]. The addition of the rare earth ions with optical activity in bismuth layer structure brings the possibility of new research as luminescent material of high performance [3]. Near-infrared to visible upconversion (UC) is an important approach for the generation of visible luminescence. More recently, the interest in upconversion emission has been increased due to the needs for all-solid compact laser devices and three-dimensional displays. Trivalent rare earth ions such as Pr^{3+}, Ho^{3+} and Er^{3+} are doped as emission centers in upconversion materials. Among these rare earth ions, the Er^{3+} ion is the most popular as well as one of the most efficient ions because the metastable $^4I_{11/2}$ and $^4I_{9/2}$ levels of Er^{3+} can be easily populated by commercial low-cost and high-power 980 and 800 nm laser diodes [4]. The downconversion and upconversion emission spectra of $PbTiO_3$ powders doped by Er^{3+} have been investigated [5]. Moreover, upconversion emissions of Er^{3+} doped $BaZrO_3$ and $BaTiO_3$ powders have also been reported [6, 7]. More recently, upconversion luminescence of $Bi_{3.95}Er_{0.05}Ti_3O_{12}$ film has been reported [8], however, the upconversion mechanisms and the ferroelectric properties of Er^{3+} doped BTO have yet seldom to be discussed.

In this work, structure, surface morphology, strong upconversion luminescence and ferroelectric properties in BTO materials doped with different Er^{3+} contents were

investigated. The effects of concentrations of Er^{3+} on the upconversion emissions and the upconversion mechanisms have been systematically discussed. The results open the possibility of ferroelectric photoluminescent (PL) materials in the application of both memories and displays.

2 Experimental procedure

$Bi_{4-x}Er_xTi_3O_{12}$ (BETO) powders with $x = 0.05$, 0.1, 0.2, 0.3, 0.4 and 0.5 were synthesized by a sol–gel process. Er^{3+} doped $Bi_4Ti_3O_{12}$ precursor solutions were synthesized using $Bi(NO_3)_3{\cdot}5H_2O$, $Er(NO_3)_3{\cdot}5H_2O$, and $Ti(OC_4H_9)_4$ were used as the Bi, Er and Ti sources, respectively. $Bi(NO_3)_3{\cdot}5H_2O$ was 10% excess in the solutions to compensate for the Bi loss during the thermal annealing. Glacial acetic acid and acetylacetone were used as cosolvents and stabilizer, respectively. The solutions were stirred for 2 h and adjusted to 0.1 M. The solutions were dried at 90 °C for 48 h, and then calcined at 750 °C in air for 3 h by a conventional muffle furnace to get the powders. The crystal structure of the powders was investigated by X-ray diffraction (XRD) on a DX-2500 X-ray diffraction apparatus with Cu Kα radiation (1.54056 Å). The surface morphology of the ceramics was examined using scanning electron microscopy (JSM5600LV). Raman spectra were recorded by a confocal microscopic Raman spectrometer (Renishaw RM-1000) with a 457.5 nm solid state laser. Visible upconversion emission spectra were measured using a SBP500 luminescence spectrometer with a PMTH-S1-CR131 photomultiplier detector and a 980 nm laser as the excitation source. To measure the ferroelectric property, the dry powders were pressed into a ceramics pellet with a diameter of 10 mm and thickness of 1 mm, then sintered at the temperature of 1,100 °C for 3 h in air. All the measurements were carried out at room temperature.

3 Results and discussion

The formation of crystalline phases was confirmed by powder XRD measurements. Figure 1a shows the XRD patterns of BTO doped with different concentrations of Er^{3+}. All the intense diffraction peaks can be indexed on the basis of a bismuth layered perovskite orthogonal phase (JCPDS, PDF#35-0795). No impurity phases was observed within the limitation of X-ray difframeter, indicating the Er^{3+} ions are effectively built into the host lattice. Based on XRD data, the lattice parameters (a, b, c) and cell volume (V) of BETO were calculated, which were shown in the Fig. 1b. The value of a, b, c and V decreased with increasing Er^{3+} content. The variations of lattice parameters and cell volume can be ascribed to the substitution for larger ion radius Bi^{3+} (0.103 nm) by smaller Er^{3+} ion (0.088 nm) in the BTO lattice.

The Raman spectra of BTO powders with different Er^{3+} contents were displayed in Fig. 2. The spectra exhibit intense phonon modes at about 268, 538 and 850 cm^{-1}, together with some weak features. The characteristic modes can be labelled according to the assignments of the Graves et al. [9]. These modes can be classified into two groups. Those at about 226, 324, 348, 538 and 560 cm^{-1} belong to B_{2g} or B_{3g} symmetry originating from the lifting of Eg degeneracy [10]. When x is over 0.3, the split between B_{2g} and B_{3g} modes (324 and 348 cm^{-1}, 538 and 560 cm^{-1}) decreases. Similar combination behaviors were recorded in the Raman spectra of simple perovskite $CaTiO_3$ with increasing temperature and BTO with increasing La content [11, 12]. This composition-dependent mode behavior is associated with the structure distortion caused by Er^{3+}doping [12]. Therefore, it is suggested that structure distortion in the BETO lattice became larger when the concentration of Er^{3+} ions is more than 0.3 mol%. Other modes at about 268, 614, and 850 cm^{-1} are due to the stretching of the TiO_6 octahedron and could be assigned as A_{1g} character [10, 11]. Raman selection rule allow 24 Raman active modes for orthorhombic BTO [13]. However, the amount of modes of all the samples can not obey the selection rule, which is partially due to possible symmetry breaking, distortion of TiO_6 octahedron and low peak intensity as well as overlap of vibration modes [14]. Referred to the assignment of BTO single crystal [15], the peak at about 850 cm^{-1} was attributed to the symmetric Ti–O stretching vibration, while the 614 cm^{-1} to asymmetric vibration. The 226 and 268 cm^{-1} modes were ascribed to the O–Ti–O bending vibration. The modes at 324 and 348 cm^{-1} were from a combination of the stretching and bending vibrations. The two modes at 538 and 560 cm^{-1} corresponded to opposing excursions of the external apical oxygen atoms of the TiO_6 octahedra. The appearance of 268, 538, and 850 cm^{-1} indicates the presence of layer perovskite structure, which was also verified by the XRD measurements [16]. Usually, the peak at 226 cm^{-1} is Raman inactive, it is observed under the current circumstances because of the distortion of the TiO_6 octahedron [15]. Raman scattering measurement is more sensitive to the structure and crystal symmetry than that of XRD measurement. As seen from Fig. 2, no peaks of impurity phase were observed besides those assigned to the phonon modes of BTO, further indicating that the Er^{3+} rare ions have effectively entered into the BTO lattice.

Figure 3 gives the SEM micrographs of the BETO ceramics. It is clearly seen that the samples ($x = 0.1$ and 0.3) exhibit plate-like grains, overlapping one another. The plate-like grains have an average thickness of approximately 600 nm, and they are random orientation according

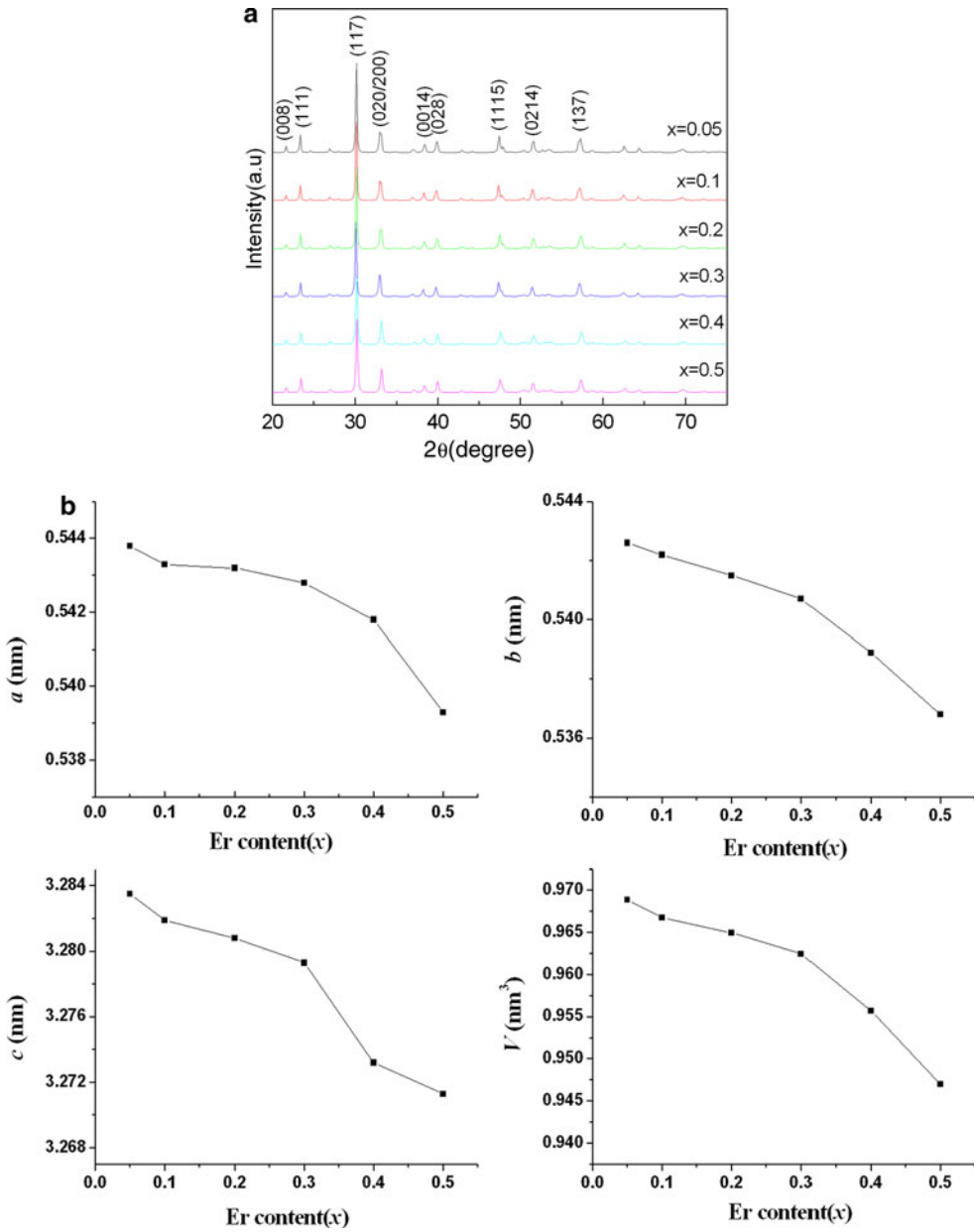

Fig. 1 **a** XRD patterns of $Bi_{4-x}Er_xTi_3O_{12}$ powders with x up to 0.5. **b** The lattice parameters (a, b, c) and cell volume (V) of BETO as functions of Er^{3+} concentrations

to XRD peaks and SEM. Such morphology is also a typical characteristic for layer structure of the Aurrivillius type [17]. The microstructure of the ceramics was varied by further increasing the Er content. It can be seen that the aspect ratio of the grains has a tendency to decrease with addition of more than 0.3 mol% of Er.

The visible emission spectra of Er^{3+} doped BTO powders under infrared excitation (980 nm) are presented in Fig. 4. For comparison, PL behavior of undoped BTO powders excited by a 450 W xenon lamp or 980 nm laser were measured, No PL emission was observed, which means the BTO powders are highly ordered at long and short-range. Similar results were also found for the BTO powders [18]. As seen from Fig. 4, the spectra of all the samples exhibit three distinct emission bands. The peaks in the green region of 525–534 nm and 545–555 nm are assigned to the $^2H_{11/2} \rightarrow {}^4I_{15/2}$, $^4S_{3/2} \rightarrow {}^4I_{15/2}$ of Er^{3+} ions, respectively, the red peak between 658 and 671 nm originates from the $^4F_{9/2} \rightarrow {}^4I_{15/2}$ transitions [19]. It has been well addressed that the green emissions are attributed to the intra spin-allowed f-f radiative transitions of Er^{3+} ions, while the red emission is attributed to another spin-allowed f-f radiative transition of Er^{3+} ions [20]. The spectra of the Er^{3+} transitions represent some discrete set of narrow lines, suggesting that the Er^{3+} occupies the crystalline site [5], which is also consistent with the experimental results of XRD and Raman. The splitting of the emission peaks is ascribed to the stark splitting of the degenerate 4f levels

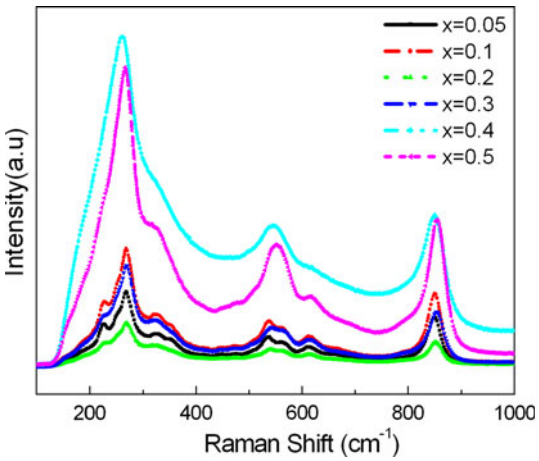

Fig. 2 Raman spectra for $Bi_{4-x}Er_xTi_3O_{12}$ powders as a function of Er content

under the crystalline fields of the host materials BTO. The green emission centered at about 550 nm is about 2–4 times as strong as the red emission centered at 662 nm, indicating that the $^4S_{3/2}$ levels are predominantly excited in these materials. It is worth noting that the upconversion fluorescence can be easily seen with naked eyes when the 980 nm diode laser is focused on the sample, even at very low pump power of the laser. The predominance of the green upconversion luminescence behavior in relation to red emission upconversion luminescence behavior was also reported in Er^{3+} doped $BaTiO_3$ powders and Er^{3+} doped $Bi_4Ti_3O_{12}$ film for excitation wavelength of 980 nm [7, 8]. While for Er^{3+} doped $PbTiO_3$ or $BaZrO_3$ perovskite powders, the green emissions ($^2H_{11/2}$, $^4S_{3/2} \rightarrow {}^4I_{15/2}$) are almost negligible and the main upconverted emissions correspond to the red band [5, 6], showing the medium have obvious influence on the photoluminescence emission of perovskites.

For the upconversion process, the UC emission intensity I is proportional to the nth power of the incident intensity P, i.e. $I \propto P^n$, where n is the number of pump photons absorbed per up-converted photon emitted. A plot of log I versus log P yields a straight line with sloped n. For the samples of various Er^{3+} concentrations, n varied from 1.65 to 2.08, indicating that two photons are participating in this UC process [6]. From Fig. 4, it is also observed that the peak intensities of the up conversion emissions of the powders increase with increasing the concentration of Er^{3+} ($x = 0.05$–0.2), and then a concentration quenching effect appeared as the $x = 0.3$. The quenching of the PL fluorescence of Er^{3+} ions would become considerable when the concentration of Er^{3+} ions further increased [21], which is associated with the formation of Er^{3+} clusters at higher Er^{3+} concentration [4]. Interestingly, the peak intensities of the upconversion emissions of the powders start to increase with the increasing x from 0.3 to 0.5. Generally speaking, the PL intensity of Er^{3+} is dependent on the structural distortion and symmetric crystal field is unfavorable for the upconversion emission because the f-f transition is originally prohibited under high spherical symmetry [22]. It should noticed that the ion radius of and Er^{3+} is smaller than that of Bi^{3+}, size-mismatch due to the substitution of Er^{3+} in the Bi^{3+} sites will increase crystal lattice distortion, and the larger the Er^{3+} content, the greater the lattice

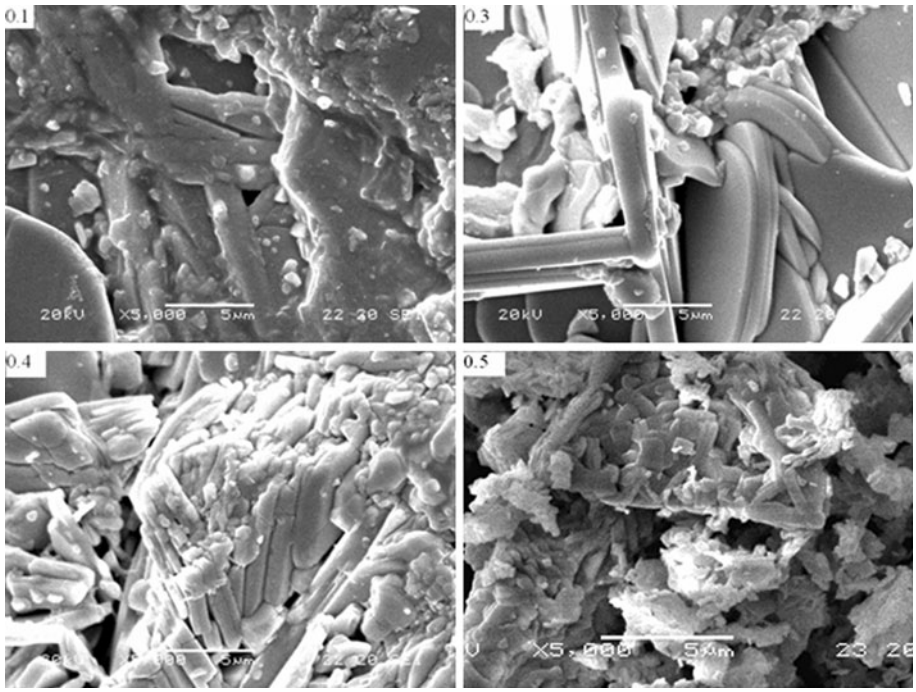

Fig. 3 SEM micrographs of $Bi_{4-x}Er_xTi_3O_{12}$ ceramics($x = 0.1$, 0.3, 0.4, 0.5)

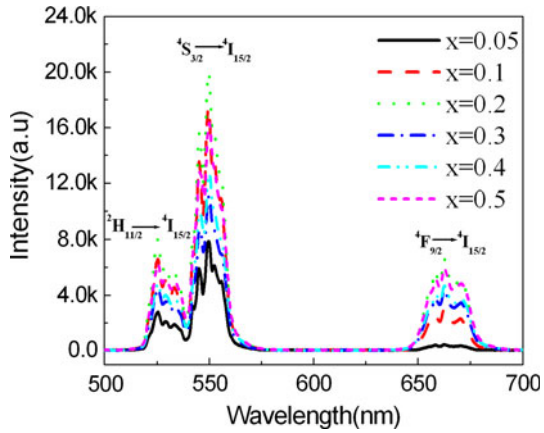

Fig. 4 Upconversion spectra of $Bi_{4-x}Er_xTi_3O_{12}$ ceramics as a function of Er content

distortion [23]. So it is inferred that as the Er^{3+} concentration further increases the additional lattice distortion accounts for an overall increase of sites with lower symmetry, giving rise to the increase in the PL intensity. From the above analysis of the Raman data, the structure distortion became larger when the x is more than 0.3 mol%, which can explain the increasing intensities of the upconversion as the x in the range of 0.3–0.5.

The mechanisms associated with the infrared-to-visible upconversion luminescence process of Er^{3+} doped oxides and oxyfluorides have been discussed in the literatures [24–26]. Although they are analogous, there are still some discrepancies due to diverse host materials. Figure 5 exhibits energy level diagram of Er^{3+} ions as well as the probable up-conversion photoluminescence mechanisms accounting for the green and red emissions. For the Er^{3+} doped BTO powders, the excitation wavelength from 980 nm matches well the absorption transition between the ground state ($^4I_{15/2}$), and the excited level ($^4I_{11/2}$). This is a ground state absorption process (GSA) [19]. After

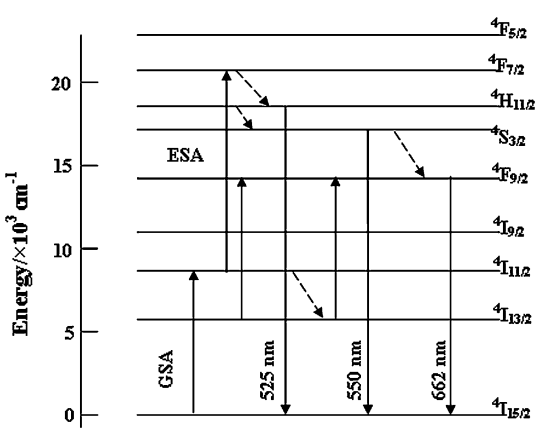

Fig. 5 Probable up-conversion photoluminescence mechanisms of the Er^{3+} doped BTO powders

first-level excitation, the Er^{3+} ions at the $^4I_{11/2}$ level may absorb a second photon and then are excited to the $^4F_{7/2}$ level. This is an excited state absorption process (ESA).The energy level diagram for the Er^{3+} ions indicates that there is a $^4F_{7/2}$ level which is approximately at twice the excitation energy of 980 nm. Moreover, two excited Er^{3+} ions at $^4I_{11/2}$ level can interact with each other through energy transfer, and one is de-excited to $^4I_{15/2}$ while the other is excited to $^4F_{7/2}$ level: $^4I_{11/2} + {}^4I_{11/2} \rightarrow {}^4I_{15/2} + {}^4F_{7/2}$. Both of the above processes can amass the ion numbers of the $^4F_{7/2}$. Afterwards, the population in the $^4F_{7/2}$ will decay non-radiatively to the $^2H_{11/2}$ and $^4S_{3/2}$ levels and the energy mismatch is compensated by the emission of phonons due to the small energy gap involved between the $^4F_{7/2}$ and $^2H_{11/2}$, $^4S_{3/2}$ levels [27]. The mechanism involved for the UC emission in the green region may be expressed as

$$\begin{aligned} &{}^4F_{7/2} \rightarrow {}^2H_{11/2}, \\ &{}^4S_{3/2} \rightarrow {}^4I_{15/2} + \text{photon in the green region} \end{aligned} \quad (1)$$

For red emission, the luminescent $^4F_{9/2}$ level can be pumped via three possible ways. Firstly, Er^{3+} ions on the $^4S_{3/2}$ level populated as pointed out previously relax nonradiatively with a moderate rate to the $^4F_{9/2}$ level. Secondly, the long living $^4I_{13/2}$ level which is nonradiative relax from the $^4I_{11/2}$ level was excited to the $^4F_{9/2}$ level by ESA process. Thirdly, a cross relaxation process between the $^4I_{13/2}$ and $^4I_{11/2}$ also contributes to the population of the $^4F_{9/2}$ level. The mechanism involved for the UC emission in the red region can be represented as

$$^4S_{3/2} \rightarrow {}^4F_{9/2} \rightarrow {}^4I_{15/2} + \text{photon in the red region} \quad (2)$$

$$^4I_{13/2} + \text{ESA} \rightarrow {}^4F_{9/2} \rightarrow {}^4I_{15/2} + \text{photon in the red region} \quad (3)$$

$$\begin{aligned} {}^4I_{13/2} + {}^4I_{11/2} &\rightarrow {}^4F_{9/2} \\ &\rightarrow {}^4I_{15/2} + \text{photon in the red region} \end{aligned} \quad (4)$$

In the above three ways, ways of (3) and (4) are dominant because of the long lifetime of the $^4I_{13/2}$ level and the quite low nonradiative relaxation probability from the $^4S_{3/2}$ level due to the large energy gap between $^4S_{3/2}$ and $^4F_{9/2}$ levels [28]. However, the process of (1) is leading since the intensity of red emissions is lower than that of green emissions for all the samples. The weaker red UC emission is also associated with the relatively small phonon energy of the BTO lattice [7].

Ferroelectricity in the BETO ceramics was performed with a radiant precision workstation ferroelectric tester at a frequency of 1 Hz and an applied voltage in the order of 7.5 kV/mm and typical ferroelectric loops were shown in Fig. 6. The loops are not fully saturated with the largest remnant polarization ($2P_r$) of 0.85 μC/cm^2. This value is

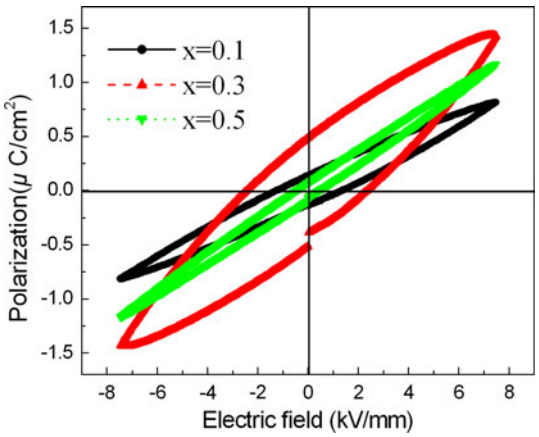

Fig. 6 *P–E* hysteresis loops of $Bi_{4-x}Er_xTi_3O_{12}$ ceramics ($x = 0.1$, 0.3, 0.5)

lower than that of pure BTO (3 μC/cm^2), comparable with Fe doped BTO ceramics and Nb doped BTO ceramics fabricated by the polymeric precursor method [29, 30]. Although the loops are lack of saturation, the loops are strong evidence to indicate that the BETO ceramics have ferroelectricity. It was found that the rare earth element Er can not improve the ferroelectric properties, which implied that Er^{3+} substituting for Bi^{3+} could not efficiently decreased the concentration of oxygen vacancies and weakened the influence of domain pining on the polarization. From Fig. 6, it is clearly that the value of $2P_r$ firstly increases and then decreases. The variation trend in $2P_r$ with the Er contents is consistent with the variation trend of grain size, which is verified by the SEM images shown in Fig. 3. The increase of grain size reduces the coupling between grain boundaries and the decrease of domain wall can appear due to more difficult reorientation and the domain wall motion [31]. Although the remnant polarization of the BETO is small, for the area of the ferroelectric gate field effect transistor is enough, because it does not need to have a large remanent polarization [32].

4 Conclusions

In summary, $Bi_4Ti_3O_{12}$ doped with different concentrations of Er^{3+} were synthesized by a sol–gel technology. The results of XRD and Raman spectra suggest that all the BETO samples consist of the Bi-layered Aurivillius phase. Results of SEM micrographs of the BETO ceramics show that the aspect ratio of the grains has a tendency to decrease with addition of more than 0.3 mol% of Er. Efficient infrared-to-visible upconversion in the Er^{3+} doped BTO powders is observed at room temperature, with generation of green emission. Three upconversion emission bands centered at about 525, 550 and 662 nm are due to the radiative relaxation of Er^{3+} from $^2H_{11/2}$, $^4S_{3/2}$ and $^4F_{9/2}$ to the ground level $^4I_{15/2}$, respectively. The $Bi_{3.8}Er_{0.2}Ti_3O_{12}$ powders have the highest relative emission intensity. The effect of concentrations of Er^{3+} on the upconversion emissions and the upconversion mechanisms has been discussed in detail. In addition, the BETO ceramics show clear ferroelectricity with the largest remnant polarization ($2P_r$) of 0.85 μC/cm^2. The results illustrate the large potential of this class of materials in integrated photoluminescence ferroelectric devices.

Acknowledgments The authors would like to thank Dr. Wenbin Su, Zhigang Gai and Minglei Zhao for ferroelectric test and helpful discussion. This work was supported by the NSFC under the grant No 50802023, Scientific and Technological Brainstorm Key Project of Henan Province (082102270039, 102102210115), the Finance Assistance Scheme of Backbone Youth Teachers in University of Henan Province (2009GGJS-026) Research Plan for Natural Science in the Education Department of Henan Province (2009A430002, 2011A430004).

References

1. Xue KH, Celinska J, Araujo CAPD (2009) Appl Phys Lett 95:052908
2. Park JH, Bae JS, Jun BE, Choi BC, Jeong JH (2007) Appl Phys A 86:63
3. Ruan KB, Chen XM, Liang T, Wu GH, Bao DH (2008) J Appl Phys 103:086104
4. Zhang XB, Wang XF, Qiao YM, Guo H (2009) Opt Mater 32:216
5. Lemos FCD, Melo DMA, da Siva JEC (2004) Opt Commun 231:251
6. Torres LAD, Salas P, Huerta JSP, Chavez CA, Rosa EDL (2008) J Nanosci Nanotechnol 8:6425
7. Zhang Y, Hao JH, Mak CL, Wei XH (2011) Opt Express 19:1824
8. Gao F, Wu GH, Zhou H, Bao DH (2009) J Appl Phys 106:126104
9. Graves PR, Hua G, Myhra S, Thompson JG (1995) J Solid State Chem 114:112
10. Hou JG, Kumar RV, Qu YF, Krsmanovic D (2010) J Nanopart Res 12:563
11. Balachandran U, Eror NG (1982) Solid State Commun 44:815
12. Wu D, Deng Y, Mak CL, Wong KH, Li AD, Zhang MS, Ming NB (2005) Appl Phys A 80:607
13. Idink H, Srikanth V, White WB, Subbarao EC (1994) J Appl Phys 76:1819
14. Zhou D, Gu HS, Hu YM, Qian ZL, Hu ZL, Yang K, Zou YN, Wang Z, Wang Y, Guan JG, Chen WP (2010) J Appl Phys 107:094105
15. Kojima S, Imaizumi R, Hamazaki S, Takashige M (1994) Jpn J Appl Phys 33:5559
16. Du YL, Chen G, Zhang MS (2004) Solid State Commun 132:175
17. Chen M, Liu ZL, Wang Y, Wang CC, Yang XS, Yao KL (2004) Phys B 352:61
18. Oliveira RC, Cavalcante LS, Sczancoski JC, Aguiar EC, Espinosa JWM, Varela JA, Pizani PS, Longo E (2009) J Alloys Compd 478:661
19. Yang J, Zhang CM, Peng C, Li CX, Wang LL, Chai RT, Lin J (2009) Chem Eur J 15:4649
20. Battisha IK, Badr Y, Shash NM, El-shaarawy MG, Darwish AGA (2010) J Sol Gel Sci Technol 53:543
21. Danilov VP, Prokhorov AM, Studenikin MI, Schmid D, Schwan LO, Glasmacher R (1999) Phys Stat Solid (a) 176:593
22. Goto K, Nakachi Y, Ueda K (2008) Thin Solid Films 516:5885

23. Pang XL, Zhang Y, Ding LH, Su ZH, Zhang WF (2010) J Nanosci Nanotech 10:1860
24. Lim SF, Riehn R, Ryu WS, Khanarian N, Tung CK, Tank D, Austin RH (2006) Nano Lett 6:169
25. Patra A, Friend CS, Kapoor R, Prasad PN, Dong YQ (2002) J Phys Chem B 106:1909
26. Wang LY, Li P, Li YD (2007) Adv Mater 19:3304
27. Singh V, Rai VK, Rak II, Watanabe S, Rao TKG, Chubaci JFD, Badie L, Pelle F, Ivanova S (2009) J Phys D Appl Phys 42:065104
28. Ma DK, Huang SM, Yu YY, Xu YF, Dong YQ (2009) J Phys Chem C 113:8136
29. Simões AZ, Aguiar EC, Ries A, Longo E, Varela JA (2007) Mater Lett 61:588
30. Chen XQ, Yang FJ, Cao WQ, Wang H, Yang CP, Wang DY, Chen K (2010) Solid State Commun 150:1221
31. Stojanovic BD, Simoes AZ, Paiva-Santos CO, Quinelato C, Longo E, Varela JA (2006) Ceram Intern 32:707
32. Fujimura N, Yoshimura T (2005) Topics Appl Phys 98:199